JGR Space Physics

RESEARCH ARTICLE
10.1029/2021JA029107

Key Points:

- The Dartmouth geomagnetic cutoff code is updated with TS07 and LFM MHD magnetic field snapshots
- The proton cutoff energy is calculated during the September 7–8, 2017 SEP event
- Comparison with data shows better correlation using LFM than TS04 and TS07

Correspondence to:
Z. Li,
Zhao.Li@Dartmouth.edu

Citation:
Li, Z., Engel, M., Hudson, M., Kress, B., Patel, M., Qin, M., & Selesnick, R. (2021). Solar energetic proton access to the inner magnetosphere during the September 7–8, 2017 event. *Journal of Geophysical Research: Space Physics*, *126*, e2021JA029107. https://doi.org/10.1029/2021JA029107

Received 21 JAN 2021
Accepted 16 JUN 2021

Solar Energetic Proton Access to the Inner Magnetosphere During the September 7–8, 2017 Event

Zhao Li[1], Miles Engel[2], Mary Hudson[1,3], Brian Kress[4,5], Maulik Patel[3], Murong Qin[6,7], and Richard Selesnick[8]

[1]Department of Physics and Astronomy, Dartmouth College, Hanover, NH, USA, [2]Los Alamos National Laboratory, Los Alamos, NM, USA, [3]Hight Altitude Observatory, National Center for Atmospheric Research, Boulder, CO, USA, [4]Center for Cooperative Research in the Environmental Sciences at CU Boulder, Boulder, CO, USA, [5]NOAA - National Centers for Environmental Information, Boulder, CO, USA, [6]Center for Space Physics, Boston University, Boston, MA, USA, [7]Cooperative Programs for the Advancement of Earth System Science, UCAR, Boulder, CO, USA, [8]Space Vehicles Directorate, Air Force Research Laboratory, Kirtland AFB, NM, USA

Abstract The access of solar energetic protons into the inner magnetosphere on September 7–8, 2017 is investigated by following reversed proton trajectories to compute the proton cutoff energy using the Dartmouth geomagnetic cutoff code (Kress et al., 2010, https://doi.org/10.1029/2009sw000488). The cutoff energies for protons coming from the west and east direction, the minimum and maximum cutoff energy respectively, are calculated every 5 min along the orbit of Van Allen Probes using TS07 and the Lyon-Fedder-Mobarry (LFM) MHD magnetic field model. The result shows that the cutoff energy increases significantly as the radial distance decreases, and that the cutoff energy decreases with the building up of the ring current during magnetic storms. Solar wind dynamic pressure also affects cutoff suppression (Kress et al., 2004, https://doi.org/10.1029/2003gl018599). The LFM-RCM model shows stronger suppression of cutoff energy than TS07 during strong solar wind driving conditions. The simulation result is compared with proton flux measurements, showing consistent variation of the cutoff location during the September 7–8, 2017 geomagnetic storm.

1. Introduction

The Earth's inner radiation belt includes an intense population of high-energy protons (10 MeV–1 GeV) trapped by the geomagnetic field below altitudes $\sim 10^4$ km. The sources of inner belt protons are cosmic ray albedo neutron decay (CRAND) and Solar Energetic Protons (Selesnick, Hudson, & Kress, 2010; Selesnick, Looper, & Mewaldt, 2007). Solar proton events consist of energetic protons emitted from the Sun or accelerated by interplanetary shocks (Reames et al., 1999). Solar protons are shielded by the Earth's magnetic field in the inner magnetosphere (Störmer, 1955). Detailed new measurements from the Van Allen Probes satellites (originally Radiation Belt Storm Probes) launched in August 2012 of both the untrapped Solar Energetic Particle (SEP) population which penetrates into around $L \sim 4$ and the trapped proton distribution at >18.5 MeV are of great value in constraining both empirical and theoretical models, and in testing theories of inner belt source, loss, and transport processes.

When the geomagnetic activity is low, the solar energetic protons are shielded by the Earth's magnetic field. Its rigidity, defined as momentum per unit charge, determines whether or not a solar proton can penetrate the shield. The cutoff rigidity is the threshold above which the proton can penetrate into the inner magnetosphere (Störmer, 1955). The cutoff rigidity depends on both the location and the particle arrival direction. The cutoff rigidity is lower for protons coming from the west, because their gyrocenters are at a larger radial distance from the earth where the magnetic shielding is weaker, while those arriving from the east must penetrate a stronger magnetic field region since their gyrocenters are within the orbit of the spacecraft (Rodriguez et al., 2010). Most previous studies focus on investigating the geomagnetic cutoff invariant latitude at low Earth orbit (Kress et al., 2010; Leske et al., 2001; Shea & Smart, 1972; Smart et al., 2010). The difference in SEP cutoffs is small for protons coming from different directions at low altitude because of their small gyroradius. Kress et al. (2004) examined solar proton access to the inner magnetosphere using observations from a highly elliptical orbit satellite. This study was limited to a single energy channel and an investigation of the cutoff for solar protons arriving from near magnetic west. Qin et al. (2019) calculated the cutoff

energy at the Van Allen Probes location for the September 11, 2017 SEP event using the TS04 magnetic field model (Tsyganenko & Sitnov, 2005) in the Dartmouth geomagnetic cutoff code Kress et al. (2010). This event was not accompanied by a geomagnetic storm. In the present study, we have improved the model applied to the September 7–8 storm interval with use of fields from both the TS07 magnetic field model (Tsyganenko & Sitnov, 2007) and the Lyon-Fedder-Mobarry global MHD simulations (Lyon et al., 2004) driven by upstream solar wind measurements. The TS07 magnetic field model compiles a new spacecraft database and uses a larger number of parameters than the TS04 model to better reproduce small magnetic field variations and equatorial currents. The LFM magnetic field model is a 3-D global self-consistent MHD model that simulates the Earth's magnetosphere in response to the upstream solar wind parameters by assuming single-fluid ideal MHD. This model is coupled to the Rice Convection Model (RCM) in the present study to better model ring current dynamics during a geomagnetic storm event (Pembroke et al., 2012; Wiltberger et al., 2017).

In this study, we focus on the September 7–8, 2017 CME shock driven event, described in Section 2. The calculation of proton cutoff energy along the Van Allen Probes trajectory and comparison with measurement is presented in Section 3, followed by discussion in Section 4.

2. September 7–8, 2017 Event

The GOES-16 Solar and Galactic Proton Sensor (SGPS) measured 1–500 MeV proton fluxes shown in Figure 1 during September 4–8, 2017. Figure 1 (top) plots flux from the west-facing SGPS unit (Dichter et al., 2015). The period shown includes SEP events beginning at 22:00 UT on the fourth and 12:00 UT on the sixth, as seen most clearly in higher energy channels. The arrival of CME shocks at Earth near 00:00 UT on both September 7 and 8 are prominent at lower energies but extend up to 150 MeV. A third increase in SEP flux occurred shortly after 00:00 UT on September 8, which is impulsive in nature (Filwett et al., 2020) versus gradual like the two SEP flux increases associated with arrival of the CME shocks (Reames et al., 1999). Other solar wind parameters, geomagnetic indices and the magnetopause location calculated using the Shue et al. (1998) model are plotted in the bottom panels. The strong increase in solar wind dynamic pressure Pdyn and weakly negative IMF Bz on September 7 produced strong inward motion of the magnetopause (middle panel). Strongly negative IMF Bz and accompanying Sym/H, which reached a minimum of −124 nT, controlled the magnetopause location on September 8 without a strong change in Pdyn.

2.1. Van Allen Probes Proton Flux Measurement

The Van Allen Probes launched in August 2012 have low inclination orbits (10.2°) across L shells between 1.1 and 5.8, providing proton measurements near the equatorial plane over much of the inner magnetosphere (Mauk et al., 2012). The orbit period is 9 h, with 11 s spin period. Figure 2 shows the two spacecrafts' orbit between September 7 and 9, with the red and blue dots showing the location of spacecraft A and B at 00:00 UT on September 8, respectively. The Relativistic Electron Proton Telescope (REPT; Baker, Kanekal, Hoxie, Batiste, et al., 2013; Baker, Kanekal, Hoxie, Henderson, et al., 2013) from the Energetic Particle, Composition, and Thermal Plasma Suite (Spence et al., 2013) can measure proton flux with energy from 20 to 200 MeV. Figure 3 shows the 21.2 MeV proton flux measured by Van Allen Probes (The data at $L < 3$ are from radiation belt protons). Dark blue data points show the pre-storm flux profile. The spin-averaged flux on both Probe A and B shows an increase at $L > 4$ after the first shock arrival near 00:00 UT on September 7. There is another sudden increase down to lower $L \sim 3.5$ at the beginning of September 8 as IMF Bz decreases to −30 nT southward and some protons are trapped near $L = 3$ for hours. Multiple peaks versus L observed by spacecraft B are due to temporal variations in the interplanetary proton flux measured at L1 (Filwett et al., 2020), also seen in GOES-16 in Figure 1 and detected by Van Allen Probes as it transits different L values. Spacecraft A is separated from B by approximately half an orbit, see Figure 2, and was located closer to perigee when interplanetary flux variations were detected by spacecraft B closer to apogee.

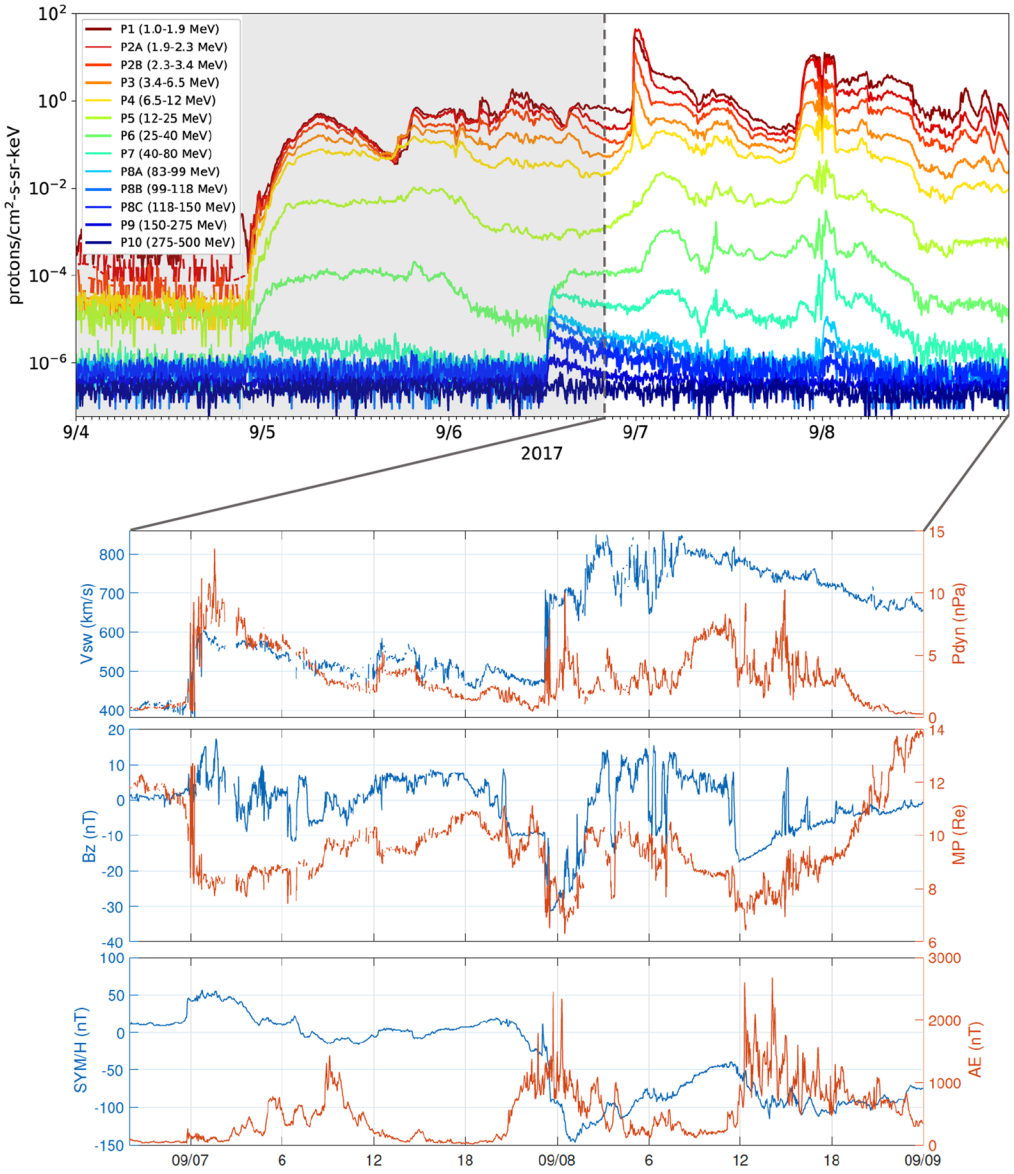

Figure 1. (Top) SEP flux measured by the west-facing SGPS instrument on GOES-16; (bottom) Solar wind parameters, geomagnetic indices from OMNI web and the magnetopause location calculated using the Shue et al. (1998) model for the September 7–8, 2017 event.

3. Simulation

3.1. Magnetic Field Model

Three magnetic field models were considered for cutoff calculations: TS04, TS07, and 5-min interval snapshots from global MHD simulations. The TS04 and TS07 empirical models are described in Tsyganenko and Sitnov (2005) and Tsyganenko and Sitnov (2007), both available at NASA SPEDAS (http://spedas.org/wiki/index.php?title=Magnetic_Field_Models_in_the_SPEDAS_GUI). The Lyon-Fedder-Mobarry (LFM) MHD model uses solar wind parameters measured near the L1 orbit propagated to the upstream boundary at $x = 30$ Re. The inner boundary of LFM is set to be 2 Re and IGRF fields are used in the region inside the LFM inner boundary in this study. The Rice Convection Model (RCM) is coupled to the LFM model to include ring current drift physics not present in ideal MHD (Pembroke et al., 2012; Wiltberger et al., 2017). A $Kp = 5$ plasmasphere model (Gallagher et al., 1988) is included as the lowest energy channel of the Rice Convection Model. A comparison of magnetic field models with measured magnetic field from the

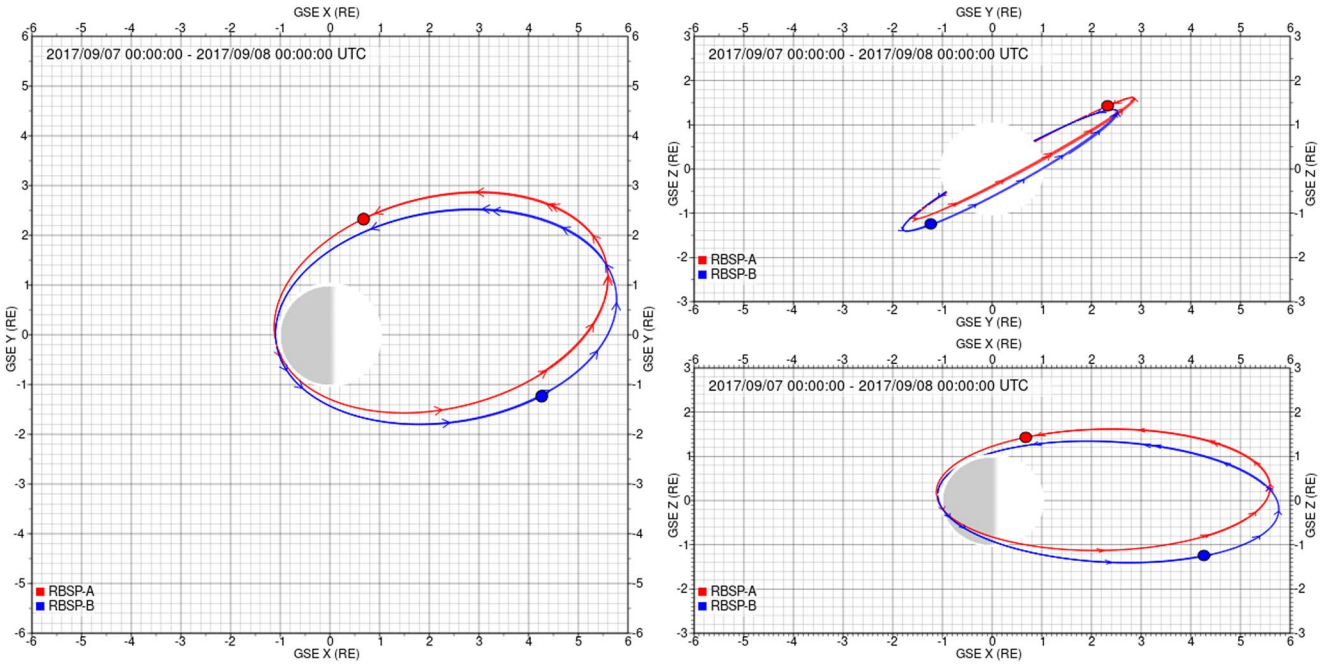

Figure 2. Van Allen Probes orbit on September 7, 2017. The left panel shows the GSM *x*-*y* plane, upper right shows *y*-*z* plane and lower right shows *x*-*z* plane.

EMFISIS instrument on Van Allen Probes (Kletzing et al., 2013) is given in the Appendix. It is seen that LFM better represents the storm time ring current in Figure A1 than either TS04 or TS07. We chose TS07 for comparison with LFM to avoid the anomalous x-line apparent in TS04 in Figure A2.

3.2. Calculation of the Cutoff Energy

To study the solar energetic proton's access into the inner magnetosphere, the Dartmouth geomagnetic cutoff code (Kress et al., 2010) is run along the path of the Van Allen Probes spacecraft during the September 7–8, 2017 event. The code computes the time-reversed proton particle trajectory in a static magnetic configuration calculated using the TS07 or LFM magnetic field model and the IGRF model inside the LFM inner boundary at $L = 2$. The input file specifies the location where the proton is launched and the direction in which it comes from. The bisection searching algorithm is used to find the cutoff rigidity at a given location, with lower bound at 0.5 MeV and upper bound at 1,800 MeV. If the proton can escape the magnetosphere (the boundary is defined at $r = 15.8$ Re) by a certain time, defined as the tmax parameter in the code, then its rigidity is considered to be higher than the cutoff rigidity at that location.

The tmax parameter defines how long the code traces the test proton trajectory to determine if it can escape the magnetosphere. If tmax is set too small, a proton might not have enough time to escape the magnetosphere even if its energy is above the cutoff energy. As a result, the calculated cutoff energy would be too high. Figure 4 shows the calculated cutoff energy versus the tmax parameter for an active (top) and quiet (bottom) time near the Van Allen Probes's apogee. Compared to tmax = 700 s, the result using tmax = 100 s overestimates the cutoff energy by 30%–50%. tmax = 100 s is used in previous studies (Kress et al., 2010; Qin et al., 2019), while tmax = 700 s is used in this study as a compromise between use of a shorter time which may overestimate cutoff energy and a longer time, for example, 1,000 s, which may overestimate the time of stationary magnetic fields.

The cutoff energy at RBSP-A and RBSP-B locations is shown in Figure 5. Red, black and blue lines indicate protons arriving from the east, vertical (radial), and west directions, respectively. Solid and dashed lines show the result using the TS07 and LFM magnetic field models, respectively. From Figure 5, we can see that the cutoff energy is highly correlated with geomagnetic activity. It decreases as Bz turns southward at 06:00 and 20:00 UT on September 7 and 12:00 UT on September 8. The cutoff energy reaches a minimum at 01:00 UT (for RBSP-B) and 13:30 UT (for RBSP-A) on September 8 when Dst is minimum with the difference af-

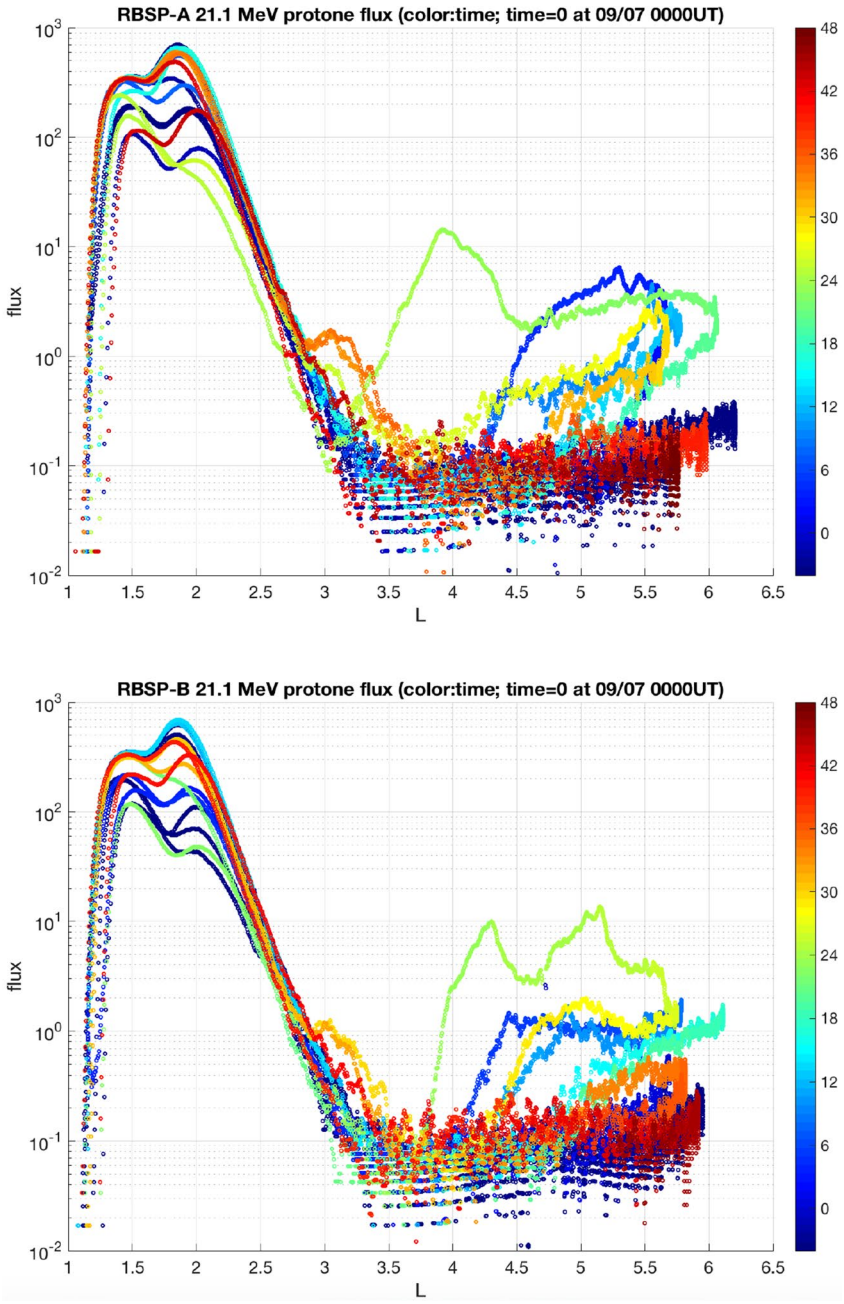

Figure 3. 21 MeV spin-averaged proton flux (unit: $cm^{-2}s^{-1}sr^{-1}MeV^{-1}$) versus L shells based on the OP77Q magnetic field model (Olson & Pfitzer, 1982) measured by Van Allen Probes A and B REPT instrument. Time is color coded (unit: hour) starting from 00:00 UT on September 7, 2017.

fected by spacecraft locations separated by roughly half an orbit in *L*, see Figure 2. The cutoff energy in the east direction is always higher than the west direction. SEPs arriving from the west have their gyrocenters at a larger radial distance from the earth where the magnetic shielding is weaker, while those arriving from the east must penetrate a stronger magnetic field region since their gyrocenters are within the orbit of the spacecraft. The cutoff energy in the vertical direction is also higher than the west direction (Rodriguez et al., 2010).

The differences between the cutoff energy in the three directions depends on the geomagnetic activity level and corresponding solar wind driving conditions. They are larger when it is quiet and smaller during disturbed times, due to the distorted magnetic field configuration. At a location in the magnetosphere, the

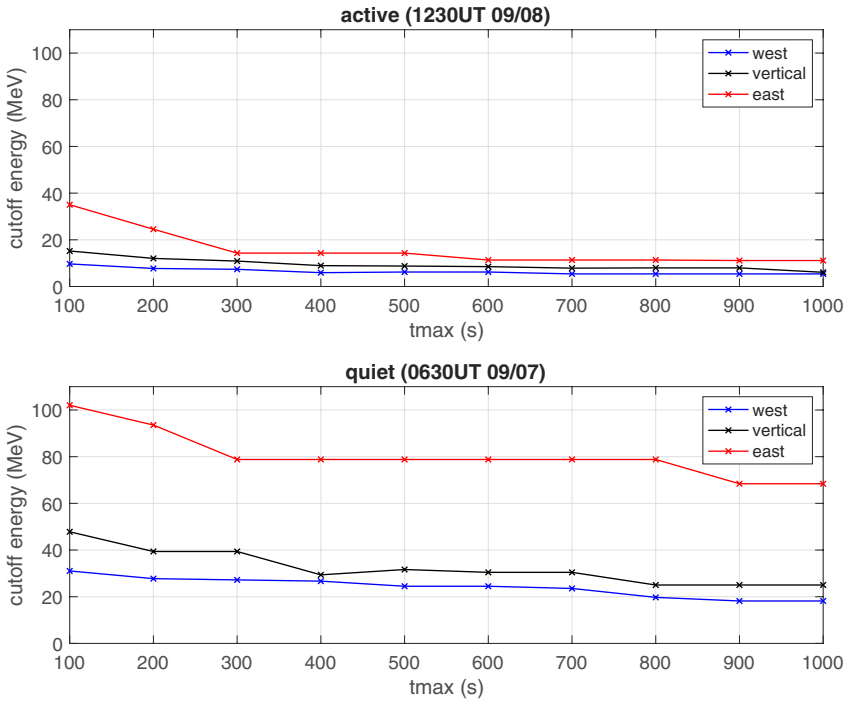

Figure 4. Calculated cutoff energy using different tmax parameters at active (top) and quiet (bottom) times.

highest and lowest cutoffs may not lie exactly along the east-west axis due to axial asymmetry of the magnetosphere. During geomagnetically disturbed periods, we expect greater deviation of the highest and lowest cutoff directions from the east-west axis. In this work, we take the SM coordinates magnetic east and west cutoffs as an approximate maximum and minimum for cutoffs for comparison with the maximum and minimum cutoffs observed within the REPT detector field of view averaged over the spacecraft spin cycle. The bottom panel of Figure 5 repeats IMF Bz, SYM/H, and the Shue magnetopause location from Figure 1. The cutoff energy is suppressed at a given location when the magnetic field is weakened by buildup of the stormtime ring current as evident in SYM/H (Leske et al., 2001). It is also apparent that solar wind dynamic pressure, which compresses the dayside magnetopause, plays a role in suppressing the cutoff energy (Kress et al., 2004).

The difference between results using the two magnetic field models, TS07 and LFM, is highly dependent on IMF Bz. The discrepancy is larger when Bz is southward, likely due to the underestimation of the ring current in TS07, better represented by the coupled LFM-RCM model as compared directly with measurement in Appendix A. When Bz is northward, for example, 12:00 to 20:00 UT on September 7 and 06:00 to 12:00 UT on September 8, the two models are very close since the magnetosphere is not so strongly distorted as it is for southward Bz.

3.3. Comparison With Van Allen Probes Measurements

Kress et al. (2010) estimated the cutoff location for a certain energy channel by finding the location where the spin-averaged flux is 50% of the flux at the satellite's apogee. We adopt this criterion for the 21 MeV energy channel to find the cutoff location from the 21 MeV spin-averaged flux measured by REPT (Figure 6 solid lines), and then compare with the simulated cutoff location, where the cutoff energy in the vertical direction is 21 MeV (Figure 6 dotted lines (top panel: TS07 fields; bottom panel: LFM)). Spin sector-resolved differential flux from the REPT instrument on Van Allen Probes is available in 36 equal angular sectors per spin. This allows for more accurate determination of the east-west flux anisotropy (Qin et al., 2019) than determining east-west from ±45° above and below the GSE *x*-*y* plane as was done by Filwett et al. (2020). The spacecraft spins about its nominal sunward-pointing axis, varying up to 10.5° between attitude corrections, see Mauk et al. (2012). If the detector measures a single energy, at the location where the cutoff energy in the vertical direction equals 21 MeV, 21 MeV protons coming from directions west of a plane normal to the east-west axis can penetrate in because the cutoff energy in the direction that they are coming from is lower than 21 MeV,

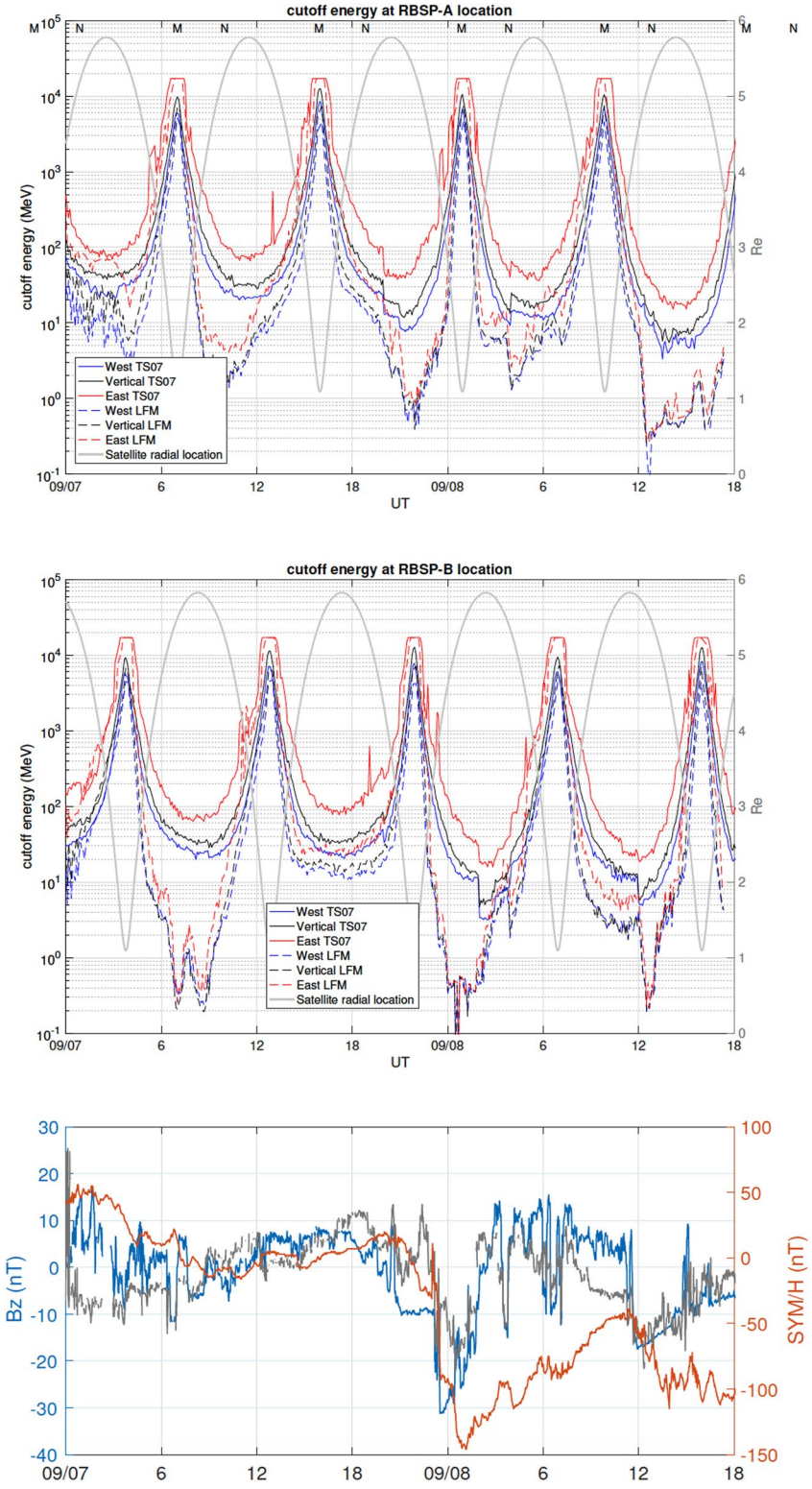

Figure 5. Simulated cutoff energy at Van Allen Probes A (top) and B (middle) location using the TS07 (solid) and LFM (dashed) magnetic field, N and M represent local noon and midnight, gray curves indicate the spacecraft location with radial position given on the right scale; (bottom) Bz, SymH, and the Shue magnetopause location (gray) from 6 to 14 Re (NASA OMNIWeb).

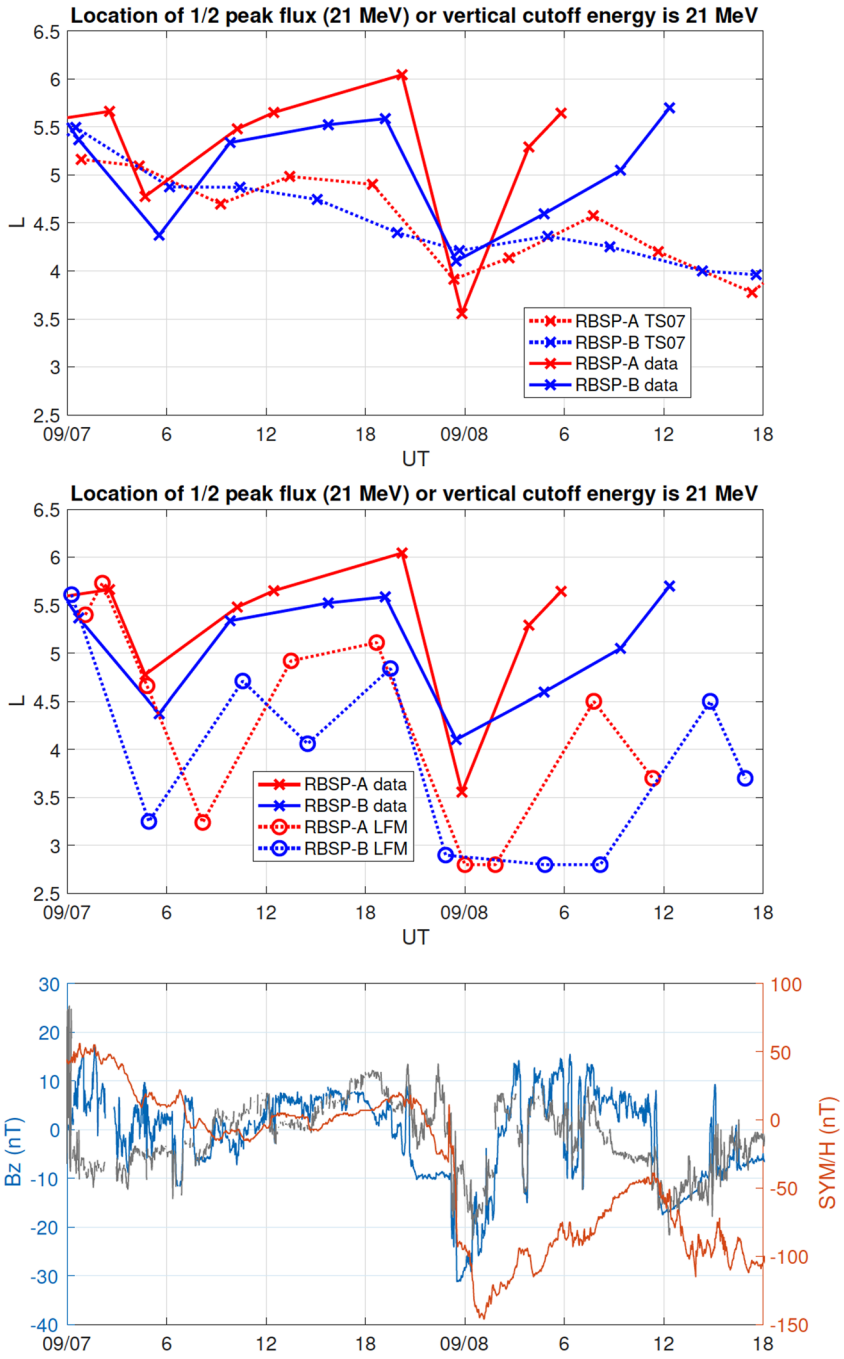

Figure 6. Location of 50% peak flux for 21 MeV energy channel (solid lines) and location where simulated cutoff energy is 21 MeV (dash lines). (a) TS07 model used for simulated cutoff; (b) LFM model used for simulated cutoff. (c) Bz, SymH, and Shue magnetopause location (gray) from 6 to 14 Re (NASA OMNIWeb).

and 21 MeV protons coming from directions east of a plane normal to the east-west axis cannot penetrate in because of higher cutoff energy. Therefore, the flux at that location is approximately 50% of the interplanetary flux, because only half of the protons (those coming from the west) can penetrate, assuming that the cutoff energy in all directions at apogee is lower than 21 MeV, which is true according to the LFM calculation.

Both measurement and simulation in the LFM fields show a decrease in cutoff L around 06:00 UT on September 7 when solar wind dynamic pressure is high and compresses the dayside magnetopause (black curve) and 00:00

UT on September 8 when IMF Bz turns strongly southward. The calculation in TS07 fields is relatively flat and has a dip at 00:00 UT on September 8. The cutoff energy calculated in LFM fields reproduces the two decreases of cutoff location in the measurement, and the magnitude of the second decrease is about the same as the measured decrease. However, the LFM simulation has a lower cutoff location overall. At the RBSP-A location, the correlation coefficient is 0.70 between measurement and the TS07 model with bias −0.49, and is 0.75 between measurement and the LFM model with bias −0.73. At the RBSP-B location, the correlation coefficient is 0.44 between measurement and the TS07 model with bias −0.33, and is 0.67 between measurement and the LFM model with bias −0.83. Cutoffs calculated with the TS07 and the LFM-RCM models bracket the observed cutoffs overall, given a dependence on finite energy bandwidth causing the measured 50% cutoffs to be higher in L than the monoenergetic cutoffs calculated with the LFM-RCM field model based on dipole considerations (Kress et al., 2013). Note that the location where the flux is half of the maximum flux is estimated based on the previous or next apogee measurement, which is changing during the Van Allen Probes 9-h period. This factor could contribute to the discrepancy between the simulation and measurement since the spacecraft measurement only determines the defined flux cutoff location for 21 MeV protons with 4.5 h half-orbit resolution. The discrepancy of the half peak flux location between the RBSP-A and B is due to the MLT dependence, see Figure 2. For example, RBSP-A was at dusk where the partial ring current is strong at 00:00 UT on September 8 which reduces the magnetic field relative to the RBSP-B pre-noon. Therefore, the cutoff energy at the RBSP-A location is lower, and the location of the half apogee flux is closer to earth compared to RBSP-B which was pre-noon.

If we take the bandwidth into consideration and assume the detector can detect protons in the energy range a to b MeV, where $a < 21 < b$, a previous study by Kress et al. (2013). Figure 1 shows that the slope of the proton cutoff energy is steeper as the angle between the arrival direction and magnetic west increases, assuming a dipole. For protons in the energy range $[a, 21]$, the range of arriving angle decreases significantly at the location where the cutoff energy in the vertical direction is 21 MeV because the cutoff energy decrease is very gradual from the vertical to the west direction. For protons in the energy range $[21, b]$, the range of arriving angle increases but not significantly at the location where the cutoff energy in the vertical direction is 21 MeV because the cutoff energy increase is very steep from the vertical to east direction. Therefore, the measured flux at the location where the cutoff energy in the vertical direction is 21 MeV is smaller than 50% of the interplanetary flux because of this asymmetry. The cutoff location calculated from the measured data should be the location where the flux is at a percentage smaller than 50% of the interplanetary flux, meaning that the solid lines in Figure 6 would be lower and closer to the dotted lines produced from the LFM model if we take the bandwidth into consideration. The calculation in Appendix B shows that this effect is negligible in this case when the bandwidth is 25% of the channel energy, so we choose to use the midpoint of the energy channel for the model calculation for consistency with several earlier works (e.g., Kahler & Ling, 2002; Kress et al., 2010). When the bandwidth is large comparing to the channel energy, this effect needs to be taken into consideration.

4. Discussion and Conclusions

In this study, we calculated the cutoff energy for energetic protons during the September 7–8, 2017 event along the Van Allen Probes orbits. The result shows that the cutoff energy decreases with the buildup of the ring current, and the suppression of geomagnetic cutoffs during a severe geomagnetic storm allows SEPs access to the inner magnetosphere. The Dartmouth geomagnetic cutoff code was used to calculate the solar energetic proton cutoff energy as a function of L, and the cutoff L at fixed energy, in both TS07 and snapshot magnetic fields from the LFM-RCM simulation of the September 7–8, 2017 geomagnetic storm. The code computes the time-reversed proton trajectory in a static magnetic field configuration. Simulated cutoff energies (lowest energy with access to a given point in space) were calculated along the orbit of the Van Allen Probes spacecraft using the two magnetic field models. The two models produce similar results when solar wind driving is weaker, in terms of dynamic pressure and negative IMF Bz. By contrast, the LFM model shows stronger suppression of cutoff energy than TS07 during stronger solar wind driving conditions, indicating greater distortion of the magnetosphere in the MHD model, also evident in direct comparison of model fields with measurements from the EMFISIS instrument on Van Allen Probes during this event, see Figure A1. When compared with Van Allen Probes proton flux measurement (Figure 6), the two models are found to bracket cutoff suppression in L at fixed energy for both enhanced solar wind dynamic pressure, which compresses the dayside magnetopause, and increased ring current which weakens the magnetic shielding as measured by Sym/H (bottom panel).

In contrast to previous work focusing on the September 11, 2017 SEP event using the TS04 magnetic field model and the same cutoff calculation methods (Qin et al., 2019), the September 7–8, 2017 period had much lower interplanetary SEP fluxes (Filwett et al., 2020; O'Brien et al., 2018) but with stronger distortion of the magnetosphere. Previous simulations of SEP cutoffs are primarily based on TS04 and one low altitude study using the LFM model without coupling to RCM (Kress et al., 2010). Ours is the first cutoff study using TS07 and LFM-RCM coupling. The weakening of magnetic shielding due to the diamagnetic effect of ring current buildup is not well reproduced with the previous models. With the inclusion of the coupled RCM to the LFM, which incorporates ring current effects that modify the cutoffs, our results revealed that ring current effects play an important role in controlling the solar proton access to the inner magnetosphere during geomagnetic storms. This also gives us a better understanding of the correlation between the geomagnetic cutoff and the Dst index.

The CME shock compression of the dayside magnetopause and interval of strongly southward IMF Bz for the event studied here resulted in stronger cutoff suppression than the September 11 event (Qin et al., 2019), both in energy and L value, particularly during intervals of high solar wind dynamic pressure and strongly negative IMF Bz (Figures 1 and 5). Previous comparisons of numerically computed SEP cutoffs with observations have been performed primarily at geosynchronous altitude and in LEO during geomagnetic storms in previous studies. Our study provides a more detailed measurement of SEP cutoffs across a broad range of L shells near the equatorial plane during storms along the trajectory of the Van Allen Probes, improving our understanding of solar proton access to the magnetosphere during geomagnetic storms.

Appendix A: Choice of Magnetic Field Models

Figure A1 shows the comparison of external Bz in TS04, TS07 and LFM magnetic field models with Bz measured by EMFISIS instruments on board Van Allen Probes A and B. TS04 and TS07 have a gradual curve and do not capture the storm time ring current well. LFM has a clear decrease from 5 to 3.5 Re, but overes-

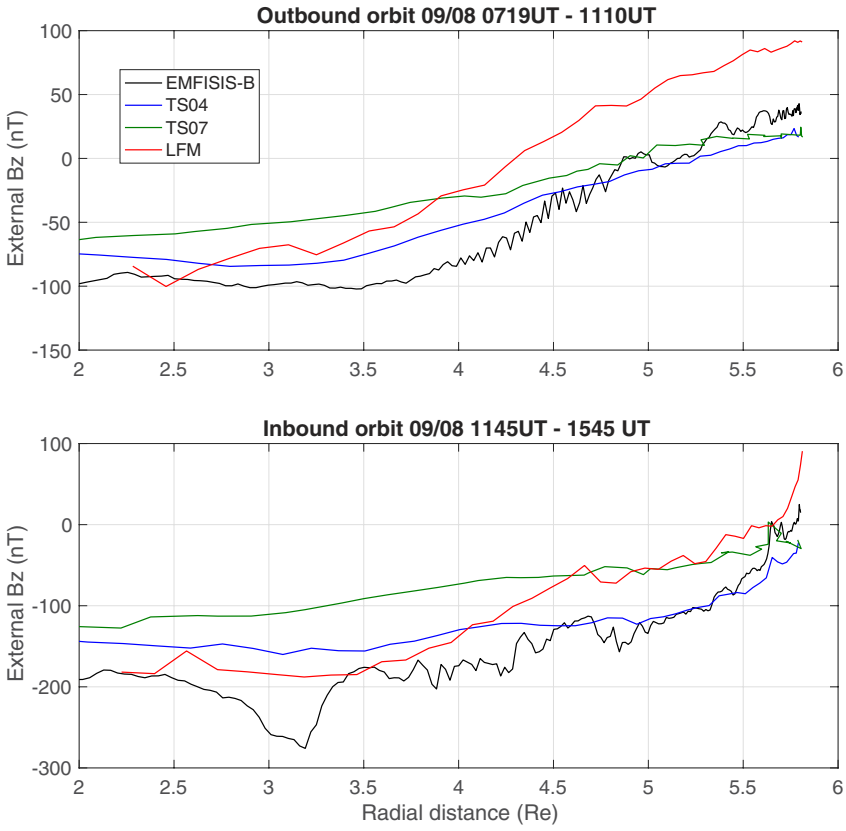

Figure A1. Comparison of external Bz in TS04 (blue), TS07 (red), and LFM (red) magnetic field models with EMFISIS measurement (black) at the location of RBSP-B for two orbits on September 8.

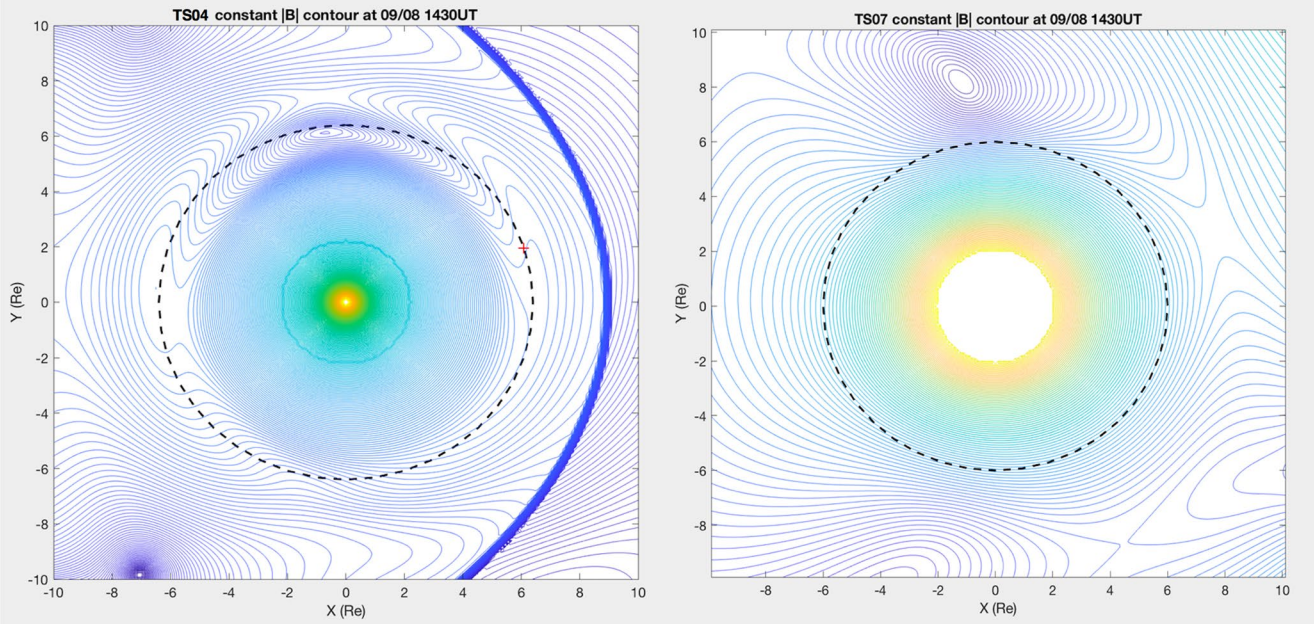

Figure A2. Constant B contour at 14:30 UT on September 8 in TS04 (left) and TS07 (right) magnetic field models.

timates the external magnetic field overall. We see artificial "X" lines in TS04 model in our simulation time interval (Figure A2) and chose TS07 and LFM model over TS04.

Appendix B: SEP Flux Rolloff With L–Shell in a Pure Dipole Magnetic Field

In this appendix, the following questions are addressed.

1. Is the vertical proton cutoff energy at the location of 1/2 interplanetary flux approximately the same as the detector channel energy?
2. If not, what is the difference in L-shell between where we observe 1/2 interplanetary flux and where the vertical proton cutoff energy is the same as the detector channel energy?

First the case with an ideal, infinitesimally narrow energy channel bandwidth is considered. Then the effect of a finite energy channel bandwidth is shown. The first three results in the subsections below address question 1. The fourth result addresses question 2.

The effect of geomagnetic cutoffs on SEPs incident on the magnetosphere is to produce a step function in the directional flux at the cutoff (Kress et al., 2013; Section 3, first paragraph and references therein). Assuming a homogeneous and isotropic SEP flux distribution in interplanetary space, $j_{IP}(E)$, the flux in the magnetosphere is modeled

$$j(E,\mathbf{r},\theta,\phi) = \begin{cases} 0 & if \quad E < E_C(\mathbf{r},\theta,\phi) \\ j_{IP}(E) & if \quad E > E_C\left(\mathbf{r},\theta,\phi\right) \end{cases} \tag{B1}$$

where the proton cutoff energy, $E_C(\mathbf{r},\theta,\phi)$, is dependent on location in the magnetosphere, $\mathbf{r}$, and direction of arrival of the incident ions, here specified by polar and azimuthal angles θ and ϕ. For convenience, we interchangeably refer to cutoff rigidity and an equivalent proton cutoff energy, $E_C = 1\times10^3 c^2(\sqrt{m_p^2 + R_C^2} - m_p)$ MeV, with proton mass $m_p = 0.93$ MeV/c^2 and R_C in GV.

Flux versus L plots like the ones shown in Figure 3 are common in studies of solar particle access to the inner magnetosphere. The theoretical description of geomagnetic shielding (Equation B1) implies that there will be a step function in the directional flux of monoenergetic ions at some radial distance. In practice, there are a number of factors contributing to a rolloff in flux with L-shell, including detector field of view

(FOV), energy channel bandwidth, temporal variations in the interplanetary flux and/or cutoff convolved with the spacecraft orbit, etc.

In comparisons between observed and numerically modeled cutoffs, a common practice is to take the location where the observed solar proton flux falls to one-half its interplanetary value as the location where the detector channel midpoint energy is equivalent to the vertical proton cutoff energy (Kahler & Ling, 2002; Kress et al., 2010; Leske et al., 2001; Smart et al., 2010). The purpose of this appendix is to show that this approach is theoretically justified.
The cutoff rigidity in a pure dipole field is

$$R_C = C_{St}\left(\frac{\cos^2\lambda}{r}\right)^2 \frac{1}{(1+\sqrt{1+\cos\alpha\cos^3\lambda})^2}, \tag{B2}$$

where r is the radial distance in units of Earth radii (R_E), λ is the magnetic latitude, α is the angle between the particle arrival direction (i.e., negative of the particle velocity) and magnetic west, and $C_{St} = 60$ is a constant containing the dipole moment and the conversion factors necessary to express R_C in units of GV (Störmer, 1955).

Solving Equation B2 for cos α yields an equation for Störmer's allowed cone expressed as a function of r, λ, and rigidity R

$$\cos\alpha = \left[\left(\frac{\cos^2\lambda}{r}\sqrt{\frac{C_{St}}{R}} - 1\right)^2 - 1\right] / \cos^3\lambda. \tag{B3}$$

This equation describes a cone of half angle α, with its axis directed westward, that encloses the allowed directions of arrival.

In the idealized case of a monoenergetic, isotropic population of ions incident on a pure dipole magnetic field, the transmissivity (e.g., see Bobik et al., 2006; Kudela & Usoskin, 2004) is the ratio of the solid angle subtended by the allowed cone to 4π

$$T = \frac{d\Omega_{allowed}}{4\pi} = \frac{2\pi\int_0^\alpha \sin\alpha d\alpha}{4\pi} = \frac{1}{2}(1-\cos\alpha) \tag{B4}$$

that is, the allowed fraction of the omnidirectional (directionally integrated) interplanetary flux. When the cutoff angle α is $\pi/2$, which includes the vertical (zenith) look direction, one-half of the interplanetary flux is allowed. Although an omnidirectional flux is used in the treatment above, it is straightforward to show that the spin-averaged flux used in this work is also at one-half its interplanetary level when $\alpha = \pi/2$, corresponding to the vertical cutoff rigidity.

Result 1. At the radial distance where the omnidirectional flux is 1/2 of the interplanetary flux, the allowed cone subtends 2π sr, and the vertical proton cutoff energy is the same as that of the measured ions.

An analytic expression for the rolloff in omnidirectional flux as a function of r, λ, and R is obtained by inserting Equation B3 into the right hand side of Equation B4

$$T = \frac{1}{2}\left(1 - \left[\left(\frac{\cos^2\lambda}{r}\sqrt{\frac{C_{St}}{R}}\right)^2 - 1\right] / \cos^3\lambda\right). \tag{B5}$$

Figure B1 shows T versus r at $\lambda = 0$ for a 100 MeV proton. Equation B5 can be empirically fit to cutoff data and used to scale omnidirectional transmissivity to different r, λ, and R. This expression provides an alternative to the Weibull distribution function, used in previous work for fitting SEP flux versus L data (Benck

et al., 2016; O'Brien et al., 2018). A similar relation adapted to detector angular and energy response can be numerically obtained as shown in Section B2 below.

Consider an ideal omnidirectional detector with effective area A_0, independent of direction and energy. The count rate is

$$C = 2\pi \int_0^{\pi} \int_{\max(E_C(\alpha),E_L)}^{\max(E_C(\alpha),E_U)} j_{IP}(E)\, A_0\, dE \sin\alpha\, d\alpha. \tag{B6}$$

The max function in the upper and lower limits of the energy integral returns the maximum of its two arguments, the directionally dependent proton cutoff energy $E_C(\alpha)$ or one of the detector channel energy channel bounds E_L or E_U. These limits restrict the energy integration interval to the portion of the channel energy bandwidth that is above the cutoff.

Using a power law to model the interplanetary spectrum

$$j_{IP}(E) = j_0 E^{-\gamma}, \tag{B7}$$

the transmissivity evaluates to

$$T = \frac{C}{C_{IP}} = \frac{\int_0^{\pi} \left(E_2^{1-\gamma} - E_1^{1-\gamma}\right)\Big|_{\max(E_C(\alpha),E_L)}^{\max(E_C(\alpha),E_U)} \sin\alpha\, d\alpha}{2\left(E_U^{1-\gamma} - E_L^{1-\gamma}\right)}. \tag{B8}$$

In the results that follow Equation B8 is numerically integrated to obtain the transmissivity as a function of r with $E_C(\alpha)$ obtained by converting Equation B2 to proton cutoff energy. T is evaluated over a range of r values to find the value of r where $T = 0.5$.

To show the effect of the finite energy channel bandwidth, we first consider an abnormally broad channel with $E_L = 50$ and $E_U = 150$ MeV and take $\gamma = 0$. In this case, Equation B8 reduces to

$$T = \frac{\int_1^{-1} \left[\max(E_C(\alpha),E_U) - \max(E_C(\alpha),E_L)\right] d(-\cos\alpha)}{2(E_U - E_L)}. \tag{B9}$$

The region of integration in Equation B9 is illustrated in Figure B2, showing proton cutoff energy versus $\cos\alpha$ at $r_{T=0.5} = 5.95\ R_E$. When $\gamma = 0$, an area in energy-$\cos\alpha$ space is proportional to its contribution to the total counts; thus, the transmissivity T is the ratio of the area between E_L and E_U above the proton cutoff energy curve (blue and green regions) to the total area between E_L and E_U (horizontal dashed lines). Since the transmissivity is 1/2, the areas A1 and A2 are equal.

Result 2. At the value of r value where $T = 0.5$, the vertical proton cutoff energy is below the channel midpoint energy. This is due to the increasing slope of the proton cutoff energy with increasing α.

Figure B3, panel (a), shows results similar to Figure B2, but with $\gamma = 2$. In this case, the lower energy region of the channel bandwidth contributes more counts than at higher energies. The radial distance where $T = 0.5$ is $r = 6.26\ R_E$, and the cutoff energy curve is at lower energies than the case with $\gamma = 0$. The area A2 is less than A1, but A2 and A1 contribute equally to the energy-$\cos\alpha$ integral.

Result 3. The effect of a negative spectral slope is to make the vertical cutoff energy further below the channel midpoint energy than in the case with $\gamma = 0$.

Figure B3, panel (b), shows the proton cutoff energy versus $\cos\alpha$ in the $\gamma = 2$ case at $r = 5.82\ R_E$, where the vertical proton cutoff energy is equivalent to the channel midpoint energy. This occurs at lower r where $T < 0.5$. The difference between the radial distance where $T = 0.5$ and where the vertical proton cutoff energy is equivalent to the channel midpoint energy is $\Delta r = 0.44\ R_E$.

Finally, using the REPT P1 channel energy bounds $E_L = 19.3$ and $E_U = 24.7$ MeV (updated from values originally published in Baker, Kanekal, Hoxie, Batiste, et al. [2013] and Baker, Kanekal, Hoxie, Henderson, et al. [2013]), in a pure dipole field at $\lambda = 0$, the radial distance where $T = 0.5$ is $r = 8.62\ R_E$. The radial distance where the vertical cutoff energy is equivalent to the channel midpoint energy is $r = 8.59\ R_E$. The difference is $\Delta r = 0.03\ R_E$.

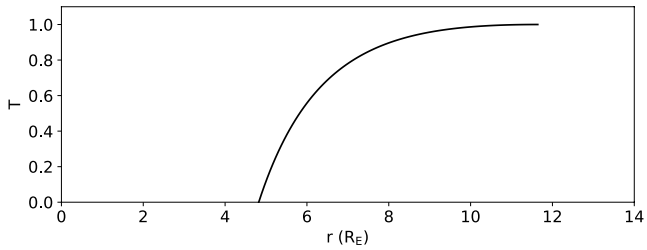

Figure B1. Transmissivity of 100 MeV protons as a function of radial distance, r, at $\lambda = 0$ in a pure dipole magnetic field with $C_{St} = 60$ GV.

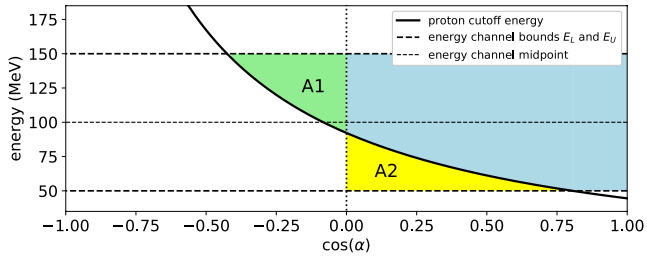

Figure B2. Proton cutoff energy versus cos α at $r_{T=0.5} = 5.95\ R_E$, in the case with $\gamma = 0$. When $\gamma = 0$, the transmissivity T is the ratio of the area between E_L and E_U above the proton cutoff energy curve (blue and green regions) to the total area between E_L and E_U (see accompanying text). Since $T = 0.5$, A1, and A2 are equal areas. The vertical cutoff energy (where cutoff curve intersects cos $\alpha = 0$) is below the channel midpoint energy due to increasing slope of the cutoff curve with increasing α.

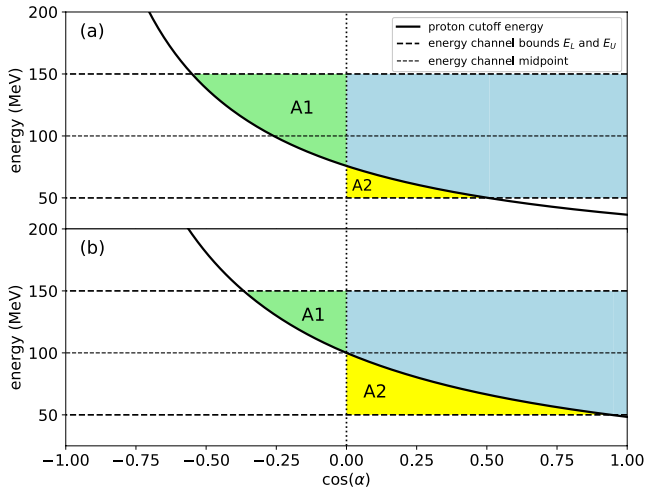

Figure B3. Panel (a): Proton cutoff energy versus cos α at $r_{T=0.5} = 6.26\ R_E$ in case with $\gamma = 2$. The area A2 is less than A1, but A2 and A1 contribute equally to the energy-cos α integral. The vertical cutoff energy is further below the channel midpoint energy than in the case with $\gamma = 0$. Panel (b): Proton cutoff energy versus cos α in $\gamma = 2$ case at $r = 5.82\ R_E$, where the vertical proton cutoff energy is equivalent to the channel midpoint energy.

Result 4. When the REPT P1 channel energy width is used (19.3–24.7 MeV), we expect the difference between the observed and modeled cutoffs due to a steep spectrum and finite energy bandwidth to be insignificant compared to other model and measurement uncertainties.

Data Availability Statement

Solar wind data can be accessed at https://omniweb.gsfc.nasa.gov. Van Allen Probe REPT/ECT data can be accessed at the website (https://www.rbsp-ect.lanl). The simulation data used to create the figures are available via Zenodo website (https://doi.org/10.5281/zenodo.4454306).

Acknowledgments
Dartmouth College and University of Colorado acknowledge support from AFOSR grant FA9550-20-1-0339. This study is also supported by NASA grant 80NSSC17K0678 and JHU/APL under NASA contracts NNN16AA09T and NNN06AA01C. The authors acknowledge high-performance computing support from NCAR CISL.

References

Baker, D. N., Kanekal, S. G., Hoxie, V. C., Batiste, S., Bolton, M., Li, X., et al. (2013). The Relativistic Electron-Proton Telescope (REPT) instrument on board the Radiation Belt Storm Probes (RBSP) spacecraft: Characterization of Earth's radiation belt high-energy particle populations. *Space Science Reviews*, *179*, 337–381. https://doi.org/10.1007/s11214-012-9950-9

Baker, D. N., Kanekal, S. G., Hoxie, V. C., Henderson, M. G., Li, X., Spence, H. E., et al. (2013). A long-lived relativistic electron storage ring embedded in Earth's outer Van Allen belt. *Science*, *340*, 186–190. https://doi.org/10.1126/science.1233518

Benck, S., Borisov, S., Cyamukungu, M., Evans, H., & Nieminen, P. J. (2016). Characterization of solar energetic H and He spectra measured by the energetic particle telescope (EPT) on-board PROBA-V during the January 2014 SEP event. *IEEE Transactions on Nuclear Science*, *63*(6), 2941–2949. https://doi.org/10.1109/tns.2016.2610520

Bobik, P., Boella, G., Boschini, M. J., Gervasi, M., Grandi, D., Kudela, K., et al. (2006). Magnetospheric transmission function approach to disentangle primary from secondary cosmic ray fluxes in the penumbra region. *Journal of Geophysical Research*, *111*, A05205. https://doi.org/10.1029/2005JA011235

Dichter, B. K., Galica, G., Mcgarity, J., Tsui, S., Golightly, M., Lopate, C., & Connell, J. (2015). Specification, design, and calibration of the space weather suite of instruments on the NOAA GOES-R program spacecraft. *IEEE Transactions on Nuclear Science*, *62*, 2776–2783. https://doi.org/10.1109/TNS.2015.2477997

Filwett, R. J., Jaynes, A. N., Baker, D. N., Kanekal, S. G., Kress, B., & Blake, J. B. (2020). Solar energetic proton access to the near equatorial inner magnetosphere. *Journal of Geophysical Research: Space Physics*, *125*, e2019JA027584. https://doi.org/10.1029/2019JA027584

Gallagher, D. L., Craven, P. D., & Comfort, R. H. (1988). An empirical model of the Earth's plasmasphere. *Advances in Space Research*, *8*, 15–24. https://doi.org/10.1016/0273-1177(88)90258-x

Kahler, S., & Ling, A. (2002). Comparisons of high latitude $E > 20$ MeV proton geomagnetic cutoff observations with predictions of the SEPTR model. *Annales Geophysicae*, *20*(7), 997–1005. https://doi.org/10.5194/angeo-20-997-2002

Kletzing, C. A., Kurth, W. S., Acuna, M., MacDowall, R. J., Torbert, R. B., Averkamp, T., et al. (2013). The electric and magnetic field instrument suite and integrated science (EMFISIS) on RBSP. *Space Science Reviews*, *179*, 127–181. https://doi.org/10.1007/s11214-013-9993-6

Kress, B., Hudson, M., Perry, K., & Slocum, P. (2004). Dynamic modeling of geomagnetic cutoff for the 23–24 November 2001 solar energetic particle event. *Geophysical Research Letters*, *31*. https://doi.org/10.1029/2003GL018599

Kress, B., Mertens, C., & Wiltberger, M. (2010). Solar energetic particle cutoff variations during the 29–31 October 2003 geomagnetic storm. *Space Weather*, *8*. https://doi.org/10.1029/2009SW000488

Kress, B., Rodriguez, J., Mazur, J., & Engel, M. (2013). Modeling solar proton access to geostationary spacecraft with geomagnetic cutoffs. *Advances in Space Research*, *52*, 1939–1948. https://doi.org/10.1016/j.asr.2013.08.019

Kudela, K., & Usoskin, I. (2004). On magnetospheric transmissivity of cosmic rays. *Czechoslovak Journal of Physics*, *54*, 239–254. https://doi.org/10.1023/B:CJOP.0000014405.61950.e5

Leske, R., Mewaldt, R., Stone, E., & Rosenvinge, T. (2001). Observations of geomagnetic cutoff variations during solar energetic particle events and implications for the radiation environment at the Space Station. *Journal of Geophysical Research: Space Physics*, *106*, 30011–30022. https://doi.org/10.1029/2000JA000212

Lyon, J., Fedder, J., & Mobarry, C. (2004). The Lyon–Fedder–Mobarry (LFM) global MHD magnetospheric simulation code. *Journal of Atmospheric and Solar-Terrestrial Physics*, *66*(15), 1333–1350. https://doi.org/10.1016/j.jastp.2004.03.020

Mauk, B. H., Fox, N. J., Kanekal, S. G., Kessel, R. L., Sibeck, D. G., & Ukhorskiy, A. (2012). Science objectives and rationale for the Radiation Belt Storm Probes mission. *Space Science Reviews*, *179*, 3–27. https://doi.org/10.1007/978-1-4899-7433-4_2

O'Brien, T. P., Mazur, J. E., & Looper, M. D. (2018). Solar energetic proton access to the magnetosphere during the 10–14 September 2017 particle event. *Space Weather*, *16*, 2022–2037. https://doi.org/10.1029/2018SW001960

Olson, W. P., & Pfitzer, K. A. (1982). A dynamic model of the magnetospheric magnetic and electric fields for July 29, 1977. *Journal of Geophysical Research*, *87*(A8), 5943–5948. https://doi.org/10.1029/JA087iA08p05943

Pembroke, A., Toffoletto, F., Sazykin, S., Wiltberger, M., Lyon, J., Merkin, V., & Schmitt, P. (2012). Initial results from a dynamic coupled magnetosphere-ionosphere-ring current model. *Journal of Geophysical Research: Space Physics*, *117*. https://doi.org/10.1029/2011JA016979

Qin, M., Hudson, M., Kress, B., Selesnick, R., Engel, M., Li, Z., & Shen, X. (2019). Investigation of solar proton access into the inner magnetosphere on 11 September 2017. *Journal of Geophysical Research: Space Physics*, *124*, 3402–3409. https://doi.org/10.1029/2018JA026380

Reames, D., Ng, C., & Tylka, A. (1999). Energy-dependent ionization states of shock-accelerated particles in the solar corona. *Geophysical Research Letters*, *26*, 3585–3588. https://doi.org/10.1029/1999GL003656

Rodriguez, J. V., Onsager, T. G., & Mazur, J. E. (2010). The east-west effect in solar proton flux measurements in geostationary orbit: A new GOES capability. *Geophysical Research Letters*, *37*. https://doi.org/10.1029/2010GL042531

Selesnick, R., Hudson, M., & Kress, B. (2010). Injection and loss of inner radiation belt protons during solar proton events and magnetic storms. *Journal of Geophysical Research: Space Physics*, *115*. https://doi.org/10.1029/2010JA015247

Selesnick, R. S., Looper, M. D., & Mewaldt, R. A. (2007). A theoretical model of the inner proton radiation belt. *Space Weather*, *5*. https://doi.org/10.1029/2006SW000275

Shea, M. A., & Smart, D. F. (1972). Secular variation in cosmic ray cutoff rigidities. *Journal of Geophysical Research*, *75*, 3921–3922.

Shue, J.-H., Song, P., Russell, C. T., Steinberg, J. T., Chao, J. K., Zastenker, G., et al. (1998). Magnetopause location under extreme solar wind conditions. *Journal of Geophysical Research: Space Physics*, *103*, 17691–17700. https://doi.org/10.1029/98JA01103

Smart, D., Shea, M., & Flückiger, E. (2010). Magnetospheric models and trajectory computations. *Space Science Reviews*, *93*, 305–333. https://doi.org/10.1023/A:1026556831199

Spence, H. E., Reeves, G., Baker, D., Blake, J., Bolton, M., Bourdarie, S., et al. (2013). Science goals and overview of the radiation belt storm probes (RBSP) energetic particle, composition, and thermal plasma (ECT) suite on NASA's Van Allen Probes mission. *Space Science Reviews*, *179*(1–4), 311–336. https://doi.org/10.1007/s11214-013-0007-5

Störmer, C. (1955). *The polar aurora*. Clarendon Press.

Tsyganenko, N., & Sitnov, M. (2005). Modeling the dynamics of the inner magnetosphere during strong geomagnetic storms. *Journal of Geophysical Research: Space Physics*, *110*. https://doi.org/10.1029/2004JA010798

Tsyganenko, N., & Sitnov, M. (2007). Magnetospheric configurations from a high-resolution data-based magnetic field model. *Journal of Geophysical Research: Space Physics*, *112*. https://doi.org/10.1029/2007JA012260

Wiltberger, M., Merkin, V., Zhang, B., Toffoletto, F., Oppenheim, M., Wang, W., et al. (2017). Effects of electrojet turbulence on a magnetosphere-ionosphere simulation of a geomagnetic storm. *Journal of Geophysical Research: Space Physics*, *122*, 5008–5027. https://doi.org/10.1002/2016JA023700